AGN feedback models: correlations with star formation and observational implications of time evolution

Robert J. Thacker,[1][⋆] C. MacMackin,[1] James Wurster[1][†] and Alexander Hobbs[2]

[1]*Department of Astronomy & Physics, Saint Mary's University, Halifax, NS B3L 3C3, Canada*
[2]*Institute for Astronomy, ETH Zurich, Zurich 8093, Switzerland*

ABSTRACT

We examine the correlation between the star formation rate (SFR) and black hole accretion rate (BHAR) across a suite of different active galactic nuclei (AGN) feedback models, using the time evolution of a merger simulation. By considering three different stages of evolution, and a distinction between the nuclear and outer regions of star formation, we consider 63 different cases. Despite many of the feedback models fitting the M–σ relationship well, there are often distinct differences in the SFR–BHAR correlations, with close to linear trends only being present after the merger. Some of the models also show evolution in the SFR–BHAR parameter space that is at times directly across the long-term averaged SFR–BHAR correlation. This suggests that the observational SFR–BHAR correlation found for ensembles of galaxies is an approximate statistical trend, as suggested by Hickox et al. Decomposing the SFR into nuclear and outer components also highlights notable differences between models and there is only modest agreement with observational studies examining this in Seyfert galaxies. For the fraction of the black hole mass growth from the merger event relative to the final black hole mass, we find as much as a factor of 3 variation among models. This also translates into a similar variation in the post-starburst black hole mass growth. Overall, we find that while qualitative features are often similar amongst models, precise quantitative analysis shows there can be quite distinct differences.

Key words: hydrodynamics – quasars: supermassive black holes.

1 INTRODUCTION

A growing body of observational evidence (for a recent review see Alexander & Hickox 2012 and references therein) suggests that the growth of supermassive black holes (SMBH) is intrinsically linked to properties of the host galaxy. Yet these relationships, be they correlations of bulge properties such as mass, luminosity or velocity dispersion relative to the black hole mass (e.g. Magorrian et al. 1998; Gebhardt et al. 2000; Ferrarese & Merritt 2000; Gültekin et al. 2009; Kormendy & Ho 2013) or the similarity of cosmological star formation rate (SFR) and black hole accretion rate (BHAR) histories (e.g. Boyle & Terlevich 1998; Silverman et al. 2008; Aird et al. 2010), are subtle and not easily understood. While at a general level numerous mechanisms are known for fuelling black hole mass growth, such as galaxy mergers (e.g. Sanders et al. 1988; Springel, Di Matteo & Hernquist 2005, hereafter SDH05; Hopkins et al. 2006), determining precise predictions for theoretical models remains a challenge because of the inherent difficulty in understand-

ing both accretion down to the SMBH scale (e.g. Shlosman, Frank & Begelman 1989; Hopkins & Quataert 2010) and the accompanying energy release ubiquitously known as active galactic nuclei (AGN) 'feedback' (e.g. Silk & Rees 1998; King 2003; Proga & Kallman 2004; Ostriker et al. 2010; SDH05).

While, as noted, there appears to be a strong correlation between the cosmological histories of SFRs and BHARs, on an individual object basis the correlation is less clear. Some observations have found positive correlations between SFRs and BHARs (e.g. Lutz et al. 2008; Serjeant et al. 2010; Bonfield et al. 2011), while others have found flat or negative correlations (Harrison et al. 2012; Page et al. 2012). However, AGN have a much shorter variability time-scale than global star formation (e.g. Hopkins & Hernquist 2009), meaning that any anticipated correlations may only become clear when averages over populations, which will capture the rapidly accreting objects, are considered. Results presented in Chen et al. (2013) for star-forming galaxies appear to provide support for this assertion. For simulation work it is possible to average over outputs taken at different times thereby averaging over different evolutionary phases.

As well as considering global star formation in galaxies, observations have also focused on whether correlations are stronger with nuclear (roughly the sub-kpc scale) or extended star formation

---

[⋆] E-mail: thacker@ap.smu.ca
[†] Present address: Monash Centre for Astrophysics, Monash University, Victoria 3800, Australia.

(e.g. Kauffmann et al. 2007; Diamond-Stanic & Rieke 2012, hereafter DSR12; LaMassa et al. 2013). As might be expected, nuclear star formation correlates more strongly with black hole accretion, while star formation in the outer regions of galaxies shows a weak correlation (at least for the sample of Seyfert galaxies considered in DSR12). For the highest luminosity systems, specifically QSOs, such a division remains beyond observational techniques.

Many models of AGN feedback implemented with galaxy formation simulations have been published (e.g. SDH05; Sijacki & Springel 2006; Thacker, Scannapieco & Couchman 2006; Okamoto, Nemmen & Bower 2008, hereafter ONB08; Booth & Schaye 2009, hereafter BS09; Debuhr, Quataert & Ma 2011, hereafter DQM11). Simulation techniques have reached the point where there is comparatively little difference between the resolved scales of simulations but once sub-grid modelling is introduced there can be significant variations between models (e.g. Wurster & Thacker 2013a,b, hereafter WT13a and WT13b, respectively; Hayward et al. 2014; Newton & Kay 2013; Ragone-Figueroa et al. 2013; Barai et al. 2014; Costa et al. 2014; Tescari et al. 2014). Incorporating the full temporal and spatial scales relevant to AGN is clearly something beyond the current capability of simulations, despite new simulations reaching impressively high resolution (e.g. Gabor & Bournaud 2013). However, the working hypothesis for the field is that resolution down to the pc level is enough to capture most of the relevant physics (e.g. Hopkins & Quataert 2010) and that augmenting sub-grid models to include different radiative behaviours of the SMBH may be the key step forward. New models which attempt to incorporate both so-called radio mode and quasar-mode feedback are now appearing (Vogelsberger et al. 2013).

To date, most simulation models have ignored the time-scales associated with accreting material on to the black hole. The accretion-disc-particle model of Power, Nayakshin & King (2011) addresses this issue partially by considering the viscous time associated with the black hole accretion disc. The original motivation of the model was to demonstrate the importance of angular momentum to the accretion process, something that Bondi–Hoyle models do not account for. While this model was originally intended for simulating accretion on pc scales, it has been shown to produce acceptable results for merger simulations (WT13a), but not cosmological (Muldrew, Pearce & Power 2013), and been further modified by Newton & Kay (2013) to incorporate the time-scale associated with material reaching the accretion disc. Along similar lines a recent preprint (Rosas-Guevara et al. 2013) has attempted to incorporate the viscous time-scale associated with accretion by considering the circularization radius to be determined by the flux of angular momentum through the smallest resolved simulation scale.

Attention has also focused on more accurately describing the accretion processes within the wider galactic potential. Hobbs et al. (2012) have demonstrated that the accretion rate can be influenced strongly by the presence of additional mass beyond the black hole (from the stellar bulge, for example, or indeed the more massive dark matter halo) when the gravitational potential energy dominates over the internal energy of the infalling gas. However, as yet, there has not been a published study of this model, and hence we undertake one as part of this investigation and include it within our comparison.

Taking all these issues together, the aim of this investigation is to extend the understanding of the SFR–BHAR correlation in context of different AGN feedback models. The specific goals are as follows.

(i) Measure the intrinsic time variation of a single merger event, and thus quantify time variation in the SFR–BHAR parameter space.

While not equivalent to ensemble averaging, it quantifies the evolutionary variation of a single AGN formation event (see Section 2 for a discussion).

(ii) Calculate the SFR–BHAR correlations for this merger, considering evolution across all the simulation, and both pre- and post-merger cases. Contrast the different models, including those with explicit accretion time-scales such as the Power et al. (2011) model, to observed correlations to see what can be inferred.

(iii) Evaluate the SFR–BHAR correlations for both nuclear and extended star formation regions to see if observational expectations are matched. Because AGN accretion and nuclear star formation are both fed by cold gas in the nuclear region stronger correlations between nuclear star formation and the BHAR are expected.

(iv) Extend our model framework to include the Hobbs et al. (2012) model in the merger context.

The layout of this paper is as follows. In Section 2 we discuss our handling of evolutionary tracks in the SFR–BHAR parameter space. In Section 3 we review the numerical methodology and simulations, and follow this with a detailed analysis in Section 4. In Section 5 we conclude with a brief review.

2 GALAXY EVOLUTION IN THE SFR–BHAR PARAMETER SPACE

As galaxies evolve their instantaneous SFR and BHAR chart an evolutionary track in the SFR–BHAR parameter space. While observationally it is only possible to reconstruct these tracks in an averaged sense (Wild, Heckman & Charlot 2010), for simulations the evolution can be plotted exactly.

What can we learn from this analysis? The key issue is generating an underlying qualitative understanding of the SFR–BHAR correlation. If galaxies track along this correlation, in both an exact or time-averaged sense tightly, then the relationship is strongly suggestive of an evolutionary explanation. If, on the other hand, the evolutionary tracks run diametrically opposite the correlation then a large intrinsic scatter is to be expected.

To put the simulation results in context it is instructive to examine what kind of behaviour in the SFR–BHAR parameter space might be expected. Let us first assume a SFR based upon a Lagrangian–Schmidt Law,

$$\dot{M}_* = C_{SFR} \rho_g^{1/2} M_g, \tag{1}$$

where C_{SFR} is dimensional constant that can be related to the star formation efficiency, M_g and M_* are the amounts of gas and stars in a given Lagrangian region and ρ_g is the gas density. For the BHAR we utilize the Bondi–Hoyle accretion formula,

$$\dot{M}_{Bondi} = \frac{4\pi G^2 M_{BH}^2 \rho_\infty}{(c_\infty^2 + v^2)^{3/2}}, \tag{2}$$

where ρ_∞ and c_∞ are the gas density and sound speed at infinity, v is the relative velocity between the gas at infinity and the black hole and M_{BH} is the mass of the black hole. Both systems are self-limiting in closed box situations. The mass in the stars, and equivalently the black hole mass, can only convert as much material as is available in a given gas reservoir.

To determine what kind of behaviour is possible, first consider early evolution in galaxies without a significant bulge, that are nonetheless gas rich. We imagine a merger will occur and form an elliptical system at a later time. Note, for simulations, the values at infinity are usually calculated as values in the vicinity of the black hole sink particle. For the outlined scenario, the M_{BH}^2 dependence

means that the BHAR will be low and evolving slowly in an absolute sense, even though the relative change in mass in a given time period, i.e. $\Delta M_{\rm BH}/M_{\rm BH}$, can be significant. The SFR at this stage is as high as it can be and the trend is towards lower SFR values with time. Hence at early stages, we expect to see small changes in the SFR and a comparatively constant, but slightly rising, BHAR producing a movement to the left and perhaps slightly upward in the SFR–BHAR space.

Jumping next to the final stages of evolution, as the gas is essentially exhausted, we can examine this under a closed box, fixed volume situation. It's also worth emphasizing that there is clearly a distinction between the nuclear gas supply and that available for star formation in the rest of galaxy. If the initial gas mass in the galaxy is $M_{\rm g_i}$, then the SFR behaviour at fixed volume is proportional to $(M_{\rm g_i} - M_*)^{3/2}$, which produces an inverse cube reduction in the SFR with time. For the BHAR, as the remaining gas mass becomes exhausted, but was initially given by $M_{\rm g_i}^{nuc}$, then the BHAR is proportional to $M_{\rm g_i}^{nuc} - M_{\rm BH}$, which produces an exponential turn-off in time. Thus at late times, or whenever nuclear gas to feed the black hole is exhausted, the slope in the SFR–BHAR parameter space can be expected to be steep due to the exponential turn-off in the BHAR.

Thus the expectation is shallow evolution at the beginning, a rising BHAR, followed by a steep turn-off. We have confirmed this behaviour by creating a toy-model of the closed box situation. Both the SFR and BHAR equations have analytic solutions, although the BHAR solution is implicit. We set the peak of the BHAR rate (which can be chosen by setting constants in the implicit solution) to occur halfway through the evolutionary period, slightly earlier but comparable to the simulations we present. We have also normalized the SFR to unity initially and chosen the mass associated with the nuclear region to be 0.01 times the mass of the galaxy. The resulting SFR–BHAR evolutionary track is shown in Fig. 1, and confirms the earlier presumptions. This model is, however, a significant oversimplification. It ignores mass flux between the galaxy and nuclear regions, the impact of self-gravity, changes in the sound speed and the impact of feedback. Nonetheless, the exponential turn-off result (in the absence of new fuel for the BH) and the early evolution towards higher BHAR values appear well motivated.
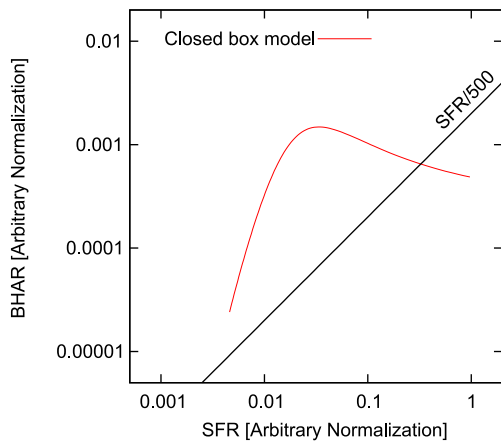
Table 1. Particle and galaxy component masses for the modelled galaxies.

Component	Total mass (10^{10} M$_\odot$)	Particle mass (10^5 M$_\odot$)	Number of particles
Dark matter halo	89.92	11.75	765 000
Hot gas halo	0.60	0.36	165 343
Stellar bulge	1.34	2.37	56 649
Stellar disc	3.56	2.37	150 375
Gas disc	0.54	0.36	150 375

It should be noted that a single merger simulation is obviously not enough to probe the SFR–BHAR correlation on an ensemble of galaxies. Current cosmological simulations (e.g. Anglés-Alcázar et al. 2013) are already comparing to the Chen et al. (2013) results, but future large-scale simulations with larger volumes (i.e. box sizes in excess of $40\,h^{-1}$ Mpc) will be able to do this analysis full justice. Once performed, they will allow a precise quantitative calculation of the scatter around the SFR–BHAR as well as potentially uncovering any expected changes in that correlation with galaxy type and age as well as cosmological redshift.

In constructing a track, the need for the inclusion of mergers means that decisions must be made on how to handle the precise definition of the pre-merger SFR and BHAR. We have chosen to take an average of the identical galaxies prior to the merger but the differences to the other methods, such as choosing just one galaxy, or adding the SFRs and BHARs, amounts to only a factor of 2 difference. Since the evolution moves through orders of magnitude changes this is not a significant issue.

Lastly, on a note of clarification, we use pre-merger to describe the systems up until 980 Myr of evolution, just at the epoch of the core merger but before a large amount of material flows into the nucleus. This means that our definition of post-merger necessarily includes data for the very highest SFRs and BHARs and might more appropriately be considered "merger and post-merger".

3 NUMERICAL MODELS

3.1 Merger and galaxy model

Full details of the galaxy models, which are Milky Way analogues, may be found in WT13b. In Table 1 we give component breakdowns of the halo, bulge and disc components of the galaxies at the fiducial resolution we consider here.

Our approach to modelling radiative cooling is the same as that of Williamson & Thacker (2012), which includes a representation of cooling down to 300 K, using the tables of Wada & Norman (2001). In all simulations, radiative cooling is implemented using an assumed metallicity of $Z = 0.05\,Z_\odot$ which means that increasing metallicity due to enrichment is not explicitly tracked. This simplifying step, which admittedly does omit some notable physics, allows us to avoid logarithmic changes in the cooling curves in small areas, which are extremely difficult to track accurately (see Thomas & Couchman 1992, for a discussion of the challenges of modelling cooling accurately in SPH calculations with strong density gradients).

3.2 Star formation

As noted in WT13b, the star formation algorithm used in all these simulations (Thacker & Couchman 2000) is kept constant to

Figure 1. Evolution of the SFR and BHAR for a closed box model of both the AGN and galaxy, plotted in the SFR–BHAR parameter space. Normalizations are arbitrary, as is the time at which the peak of the BHAR occurs, but the values have been chosen to approximately correspond to the values found in the merger simulations presented later. The SFR/500 line is included for reference with later plots (see Section 4.2).

minimize differences from one AGN feedback algorithm to another. The algorithm is based upon the 'classical' approach that enforces the SFR by utilizing a Lagrangian version of the Schmidt Law (e.g. Katz 1992; Kennicutt 1998). The method also relies upon the assumption of pressure equilibrium between ISM phases to estimate the density of local gas that should be transferred to a hotter phase under feedback. This approximate density, which is much lower than that of cold gas, is then used in the cooling function because the SPH density responds more slowly than the cooling times of high-density gas ($n_H > 1 \text{ cm}^{-3}$) at the typical feedback temperature employed (10^6 K). In practice this approach is very similar to delayed-cooling models (e.g. Stinson et al. 2006), which remain useful when simulations do no have enough resolution in the spatial or time domains to resolve energy input sufficiently accurately.

While this method is well documented in the literature, it has some notable differences to more recent approaches that rely upon effective equations of state (e.g. Springel & Hernquist 2003). Perhaps the most well-known difference is that the classical model has a stronger resolution dependence than EOS based approaches, although this must be tempered with recognition that increased resolution should allow for better capturing of local density gradients and hence the local SFR.

There are subtle differences as well. In particular, Springel et al. (2005) demonstrate that at the apoapsis of the merger there is rapid star formation in the classical approach, but not in the EOS-based version. This is due to the gas being kept dynamically hotter in the latter model, at both low and high resolution. It is also worth noting that the precise bar behaviour in these merger models is very sensitive to nuclear (bulge) masses. For example, we showed in WT13b that the inclusion of black hole tracer particles of mass 10^9 M$_\odot$ (as in the DQM model) was enough to stabilize against bar formation, while lighter tracer particles did not. This behaviour highlights the difficulty in correctly evolving instabilities in the presence of a dynamically changing potential.

Nonetheless, despite these documented differences, the SFR results we presented in WT13b are in broad agreement with the other works that used EOS-based approaches and the differences between AGN models produced notably larger impacts on the SFR values.

3.3 AGN feedback implementations

We revisit the numerical models first discussed in WT13a, WT13b and also add a new model implementing the Hobbs et al. (2012) algorithm. In our previous paper we highlighted that there are essentially five key attributes to an AGN feedback implementation:

  (i) The accretion rate on to the black hole,
  (ii) The SPH particle accretion algorithm,
  (iii) The energy feedback algorithm,
  (iv) The black hole advection algorithm, and
  (v) The black hole merger algorithm.

For completeness (additional details may be found in WT13b) we summarize salient features of each algorithm, in the context of the above attributes. It is worth emphasizing that there is a strong distinction between the numerical influence radius of the black hole, r_{inf}, often set to determine a fixed number of neighbour particles, as compared to the gravitational sphere of influence $r_h = GM_{\text{BH}}/\sigma^2$, where σ is the local velocity dispersion.

3.3.1 Model 1: SDH

This model is based upon the model found in SDH05. The accretion rate is given by a modified Bondi accretion rate,

$$\dot{M}_{\text{Bondi}} = \frac{4\pi \alpha G^2 M_{\text{BH}}^2 \rho}{\left(c_s^2 + v^2\right)^{3/2}}, \tag{3}$$

where c_s and ρ are the local sound speed and local density of the gas, and v is the relative velocity of the black hole to the nearby gas. A free parameter α, which we set to 100, is included to adjust for the limited maximum density resolved in these merger simulations. The maximum accretion rate is limited by the Eddington rate, $\dot{M}_{\text{BH}} = \min\left(\dot{M}_{\text{Bondi}}, \dot{M}_{\text{Edd}}\right)$. To accrete particles on to the black hole a 'stochastic-unconditional' algorithm is used. Particles within r_{inf} of the black hole particle are tested against a calculated probability of accretion based upon the black hole growth rate and the local density. Note that while M_{BH} denotes the mass of the black hole in the model (frequently referred to as the 'internal' mass), the actual dynamical mass in the simulation, m_{BH}, builds up over time by particle accretion and can be slightly different from M_{BH}. Of course, an accretion algorithm should ideally maintain $m_{\text{BH}} \sim M_{\text{BH}}$ (see WT13b).

Energy is returned to particles within r_{inf} using a coupling efficiency of 5 per cent and assuming an overall energy output of $\epsilon_r \dot{M}_{\text{BH}} c^2$ with the radiative efficiency ϵ set to 10 per cent. Energy is returned isotropically and is also weighted by the local SPH kernel so that particles further from the black hole particle receive less energy.

Advection of the black hole proceeds by moving the position to the gas particle with the lowest potential provided that the relative velocity between them is less than one quarter of the local sound speed. Black hole mergers occur when two black hole particles come within their mutual SPH smoothing lengths and their relative velocity is less than the local sound speed.

3.3.2 Model 2: BS

Primarily designed for cosmological volumes, this model (see BS09) builds upon the SDH implementation by modifying the α parameter to produce higher feedback when the local density goes above a threshold density, n_H^*, of 0.1 cm^{-1}. The α parameter thus becomes a function of the local hydrogen density,

$$\alpha = \begin{cases} 1 & \text{if } n_H < n_H^* \\ \left(\frac{n_H}{n_H^*}\right)^\beta & \text{otherwise} \end{cases}, \tag{4}$$

and following BS09 we have set $\beta = 1$. As with SDH the maximum accretion rate is also Eddington limited.

The feedback energy in this model is calculated in the same way as SDH, but the coupling efficiency is taken to be three times higher ($\epsilon_f = 0.15$, $\epsilon_r = 0.1$). The energy is returned to particles individually though, rather than spread over neighbours once a critical energy is reached, given by

$$E_{\text{crit}} = \frac{m_g k_B \Delta T}{(\gamma - 1) \mu m_H}, \tag{5}$$

where m_g is the (initial) mass of a gas particle and ΔT is the temperature increase a particle experiences with every feedback event. We set a lower temperature threshold of 5×10^6 K to primarily ensure stability of integrations at our mass resolution, which is appreciably higher than that used in BS09. This choice leads to more frequent but less powerful episodes of feedback, meaning that the amount of

hot gas in the halo may possibly be lower in our models. However, over the lifetime of the merger the feedback energy budgets should be similar regardless of the chosen ΔT.

Gas particles are accreted by a stochastic-conditional particle accretion algorithm. If $M_{BH} < m_{BH}$, then the probability of accretion is $p_i \equiv 0$, otherwise it is calculated using the mass difference, the local density and the kernel weight w_i, via,

$$p_i = w_i \left(M_{BH} - m_{BH} \right) \rho^{-1}. \tag{6}$$

As in Model SDH, particle i is accreted if $p_i > x_i$, where x_i is a random number.

The black hole advection is the same as in Model SDH, while two black holes are considered to have merged when they come within each other's smoothing lengths and have a relative velocity less than the circular velocity at the radius of the most massive black hole's smoothing length.

3.3.3 Model 3: ONB

This model was also originally developed (ONB08) for use in simulations using cosmological initial conditions. It is also solely focused on reproducing radio-mode feedback rather than the brighter quasar-mode so different behaviours should be expected for it, and indeed are found (WT13b). Based upon the model of Kawakatu & Umemura (2002) mass growth of the black hole is determined by radiative drag estimates on the ISM near the black hole leading to a loss of angular momentum and accretion. The net accretion rate from this drag is given by

$$\dot{M}_{drag} = \epsilon_{drag} \frac{L_{RSF}}{c^2} \left(1 - e^{-\tau_{RSF}} \right), \tag{7}$$

where $\epsilon_{drag} = 1$ is the drag efficiency, L_{RSF} is the total bolometric luminosity of all the stars in the region of star formation (RSF) near the black hole, and τ_{RSF} is the total optical depth of the RSF. Luminosities are found using PEGASE2 (Fioc & Rocca-Volmerange 1997) while the optical depth is calculated from the total mass of clouds in the RSF, its radius and the mass extinction coefficient.

Feedback in this model is directed specifically into the halo via a jet modelling approach, which also includes a distinction between jets from standard (optically thick) thin discs versus those from radiatively inefficient accretion flows, with optically thin but geometrically thick discs. Thermal energy associated with the jets is distributed to the nearest 40 gas particles below a specified density threshold.

Particles are accreted via a probabilistic approach whenever the internal mass exceeds its dynamical mass, a process we call 'continual-conditional' accretion. The black hole trajectory always heads towards the steepest stellar density via

$$\Delta l_{ONB} = \min(0.01 \epsilon_{S2}, 0.03 |v| dt), \tag{8}$$

where ϵ_{S2} is the gravitational softening length, v is the velocity of the black hole, and dt is the time-step; these coefficients are the same as in ONB08 and were determined empirically. Mergers of black holes occur when both black hole particles are within their mutual softening lengths, and are gravitationally bound.

3.3.4 Model 4: DQM

This model DQM11 uses a fundamentally different approach to accretion, and focuses on the transport of material from large scales to small via the 'instabilities within instabilities' concept and grav-

itational torques (e.g. Hopkins & Quataert 2010). The accretion rate is

$$\dot{M}_{visc} = 3\pi \delta \Sigma \frac{c_s^2}{\Omega}, \tag{9}$$

where δ is the dimensionless viscosity, Σ is the mean gas surface density, and $\Omega = \sqrt{GM/r_{inf}^3}$ is the rotational angular velocity of the gas. We set the free parameter δ to 0.05 as in DQM11.

Feedback energy is returned via a momentum approach, assuming an infrared optical depth of 10. The momentum is injected radially and isotropically on to the particles within r_{inf}. As in other models, the luminosity is limited by the Eddington rate such that $L = \min \left(\epsilon_r \dot{M}_{visc} c^2, L_{Edd} \right)$.

Black holes are modelled using tracer particles of mass $10^9 \, M_\odot$. This necessarily decouples the internal mass from any concept of a dynamical mass (as it is held fixed). The large masses of the black hole particles means they preferentially follow the local minimum of the potential. We randomly remove gas particles from the simulation that are within two smoothing lengths of the black hole to match the increase of the internal black hole mass. Mergers of black holes occur when they approach within one softening length of one another regardless of their velocity.

3.3.5 Model 5: WT

This model (see WT13b) combines a number of approaches that have appeared in the literature to draw together algorithms showing desirable behaviours (such as stability of the black hole trajectory). The modified Bondi accretion rate of SDH05 is used, but feedback energy is returned thermally using a top-hat kernel for all particles within r_{inf}. This prevents excessive heating close to the black hole.

Particle accretion is handled using a continual-conditional algorithm: When $M_{BH} > m_{BH} + m_g/2$, we accrete the gas particle that is nearest to the black hole. This keeps the internal and dynamical masses very closely coupled.

Black hole advection is broadly similar to that of ONB, but utilizes the total local potential rather than just stellar particles. The distance the black hole is displaced has been modified to

$$\Delta l_{WT} = \min(0.10 h_{BH}, 0.30 |v| dt). \tag{10}$$

Even in the presence of voids produced by winds this approach produces a smooth track for the black hole trajectory. Mergers of black holes rely upon the same approach as SDH05.

3.3.6 Model 6: PNK

The PNK model (Power et al. 2011) couples together the black hole and associated accretion disc processes. The original motivation behind the model was to address the issue that Bondi–Hoyle approaches overestimate accretion of rotationally supported cold gas discs. The model also was extended to include the viscous time-scale, t_{visc}, associated with material accreting from the accretion disc into the black hole.

Particles are accreted on to the accretion disc, of mass M_{disc}, whenever they fall within the accretion radius R_{acc}, which is typically of the order of a few pc. It is worth noting that this is of course far below the resolution scale of these simulations, so in practice R_{acc} behaves as an accretion rate limiter. The mass that is extracted is then added to the accretion disc mass, which in turn accretes on to the black hole at a rate $\dot{M}_{BH} = \min(M_{disc}/t_{visc}, \dot{M}_{Edd})$. From this accretion rate the feedback energy is returned using the same wind method as DQM. Black hole advection and mergers are handled in the same way as the WT model.

In WT13a we investigated a number of different accretion radii and viscous time-scales. To make our current analysis compact, we have decided to focus on a model that uses a 5 Myr accretion time-scale and an accretion radius that is 5 per cent of the minimum smoothing length (which essentially sets the mass flow rate on to the accretion disc). We refer to this model throughout the paper as PNK0505, although in WT13a it is labelled as PNKr05t05.

3.3.7 Model 7: HPNK

Even in the absence of significant angular momentum in accretion the Bondi–Hoyle formalism can still lead to inaccurate accretion rates, for example when gas can free-fall due to highly efficient cooling processes. Similarly the potential is assumed to be derived solely from the mass of the black hole, whereas in galaxies the surrounding halo could legitimately be expected to have an impact on the flow. Hobbs et al. (2012, hereafter HPNK12) have shown that a modification of the Bondi–Hoyle formalism to include the enclosed total mass within the smoothing radius and the impact of the associated velocity dispersion produces the interpolating formula

$$\dot{M}_{\mathrm{interp}} = \frac{4\pi\lambda(\Gamma)G^2\,M_{\mathrm{enc}}^2\rho_\infty}{(c_\infty^2+\sigma^2)^{3/2}}, \qquad (11)$$

which captures much of the desired behaviour. On small evaluation scales it approaches the Bondi–Hoyle formula while on larger ones it naturally includes the larger potential.

The smoothing radius in this model is set at the softening length of 120 pc. We also keep this particular value fixed with time, rather than relying upon a variable value to enclose a certain number of neighbours as that could potentially change by large amounts if a cavity is blown in the gas distribution during violent feedback events. As discussed in Barai et al. (2014) all black hole modelling approaches that use a variable smoothing length have the potential to develop voids, and we return to this point in Section 4.3.1.

For the feedback, black hole advection and merging algorithms we utilize those implemented in the WT model. This provides a direct means of assessing the impact of changing the mass accretion rate.

4 RESULTS

With the exception of model ONB, all the models were evolved through the merger to approximately 500 Myr afterwards, for a total simulation time of 1.5 Gyr. The ONB model was only evolved for 1.25 Gyr due to a clustering slowdown caused by the lack of feedback in this model. We still, however, provide post-merger numbers for this simulation on the basis of the smaller amount of data that we have. While the models have gravitational softenings of 120 pc, and capture variations in star formation and AGN feedback over several orders of magnitude in density, it is unlikely that they are converged with respect to small-scale variations in the SFR and AGN feedback. We have, however, shown that gross features, such as the black hole masses, do seem to be predicted well as a function of resolution in some models. Our primary focus is thus on differences between models and qualitative trends, and we caution against over-interpretation of the observational comparison.

4.1 HPNK compared to other models

We first examine the impact on the black hole mass evolution which is given in the top panel of Fig. 2. We compare to two other models, WT and BS, as the final mass of the WT model lies close to the Gültekin et al. (2009) M–σ relationship, while the BS model

has the lowest mass associated with Bondi–Hoyle type accretion models. Together these two models give a good idea of the range of masses found in WT13b. What is immediately noticeable is that the HPNK mass accretion rate has led to significant mass growth prior to apoapsis. Specifically, at apoapsis the total mass in black holes for HPNK, WT and BS is, respectively, $1.80 \times 10^6\,\mathrm{M_\odot}$, $1.15 \times 10^6\,\mathrm{M_\odot}$ and $0.67 \times 10^6\,\mathrm{M_\odot}$, making the black hole mass total almost 60 per cent higher in HPNK than WT. Examining the mass accretion rates, shown in the lower panel of Fig. 2, shows that prior to apoapsis HPNK is almost always more active than the other two models plotted, although they do not have a specific ordering between themselves, with WT sometimes having higher rates than BS and vice versa. The higher accretion rates associated with HPNK also mean that there is more feedback occurring prior to and at apoapsis.

In the period between apoapsis and second periapsis, trends are notably different. While the accretion rate for WT rises sharply up to a peak at $\sim 10^{-1}\,\mathrm{M_\odot\,yr^{-1}}$ and then falls, HPNK falls on a consistent trend to just above $10^{-3}\,\mathrm{M_\odot\,yr^{-1}}$ and BS, as a result of strong feedback, is over an order of magnitude lower at second periapsis.

As the simulated galaxies begin to reach core-merger there is an increase in accretion for all the models. As a relative fraction of mass, between core-merger and the end of the simulation the total
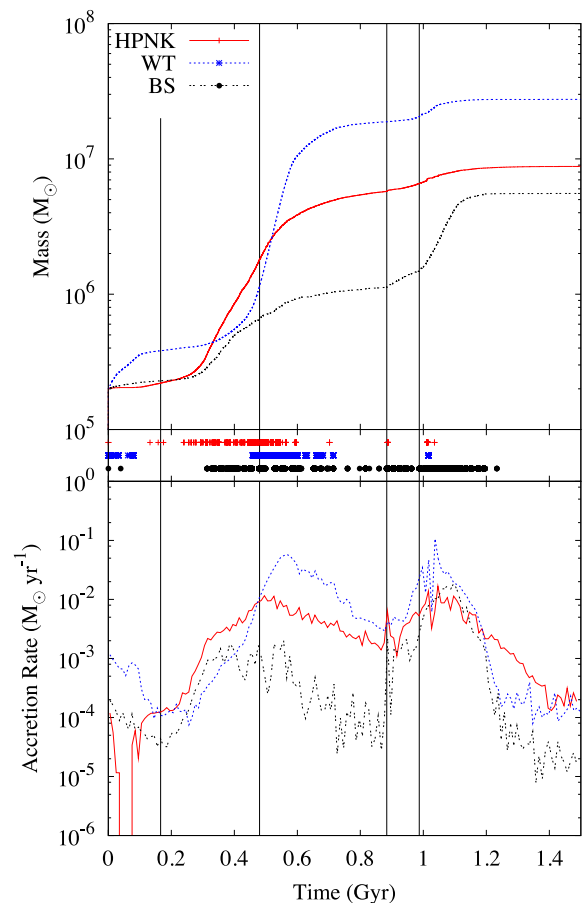

Figure 2. Total black hole mass in the simulation versus time (10 Myr bins) for the BS, WT and HPNK models (upper panel), epochs at which accretion is Eddington limited (middle panel), and the total accretion rate on to the black holes (bottom panel). The black lines indicate, from left to right, first periapsis at 166 Myr, apoapsis at 480 Myr, second periapsis at 884 Myr and the core merger at 987 Myr.

BS black hole mass grows by a factor of 2.55, while for WT the factor is 1.36, and for HPNK 1.20 (although see Section 4.4 for a more detailed discussion of all models). The final black hole mass for HPNK is $8.80 \times 10^6 \, M_\odot$ and the stellar component has an associated velocity dispersion of $144 \, km \, s^{-1}$. For this σ the mean of the Gültekin et al. (2009) M–σ predicts a final black hole mass of $3.30 \times 10^7 \, M_\odot$, and, for their quoted standard deviation, the HPNK black hole mass is approximately 1.4 standard deviations below the mean. For comparison, the BS model, which has an essentially identical velocity dispersion, is over 2.1 standard deviations below the mean, while the WT model lies essentially on the mean.

The SFR for HPNK is broadly similar to the BS model. There is only a moderate increase at both apoapsis and during the core merger, and the final stellar masses vary by only 2 per cent, with WT, BS and HPNK all being very close to $10.3 \times 10^{10} \, M_\odot$. As might be expected given the similarity in the evolution, the final morphology is also similar to the BS model with the embedded central gas disc again being very small compared to other models such as WT. The hot circumgalactic gas halo is also smaller (when measured by a visual cuts at $10^6 \, K$ and $10^5 \, K$) than WT or DQM, a result that is again similar to the BS model.

4.2 Ensemble correlations compared to time-averaged simulations and SFR–BHAR evolution

We first consider correlations of the SFR and BHAR for the entire galaxies by examining the evolutionary tracks and then taking time averages. In the absence of feedback, the closed box models discussed in Section 2 suggest that correlations in the SFR–BHAR space can become quite steep after the peak BHAR is reached. However, prior to that epoch the converse may be true, and shallow negative correlations are possible depending upon the evolutionary epoch considered. As a general rule feedback can be anticipated to shift both SFRs and BHARs to lower values, but the precise impact on the exact correlation requires evaluation from simulations.

In this analysis we follow the Chen et al. (2013) convention of correlating the SFR against the BHAR, i.e. $\log{(BHAR)} = \alpha + \beta \times \log{(SFR)}$. We also further analyse the SFR behaviour by separating it into the nuclear and extended components, and to match the prior literature analyses, switch to correlating the BHAR against the SFR.

4.2.1 Evolution tracks in the SFR–BHAR parameter space

By examining evolution in the SFR–BHAR parameter space we can gauge the overall variation between models and how this compares to observed properties such as inferred evolution (Wild et al. 2010), measured correlations of infrared selected star-forming galaxies (Chen et al. 2013), and the SFR/500 value derived from the M_{BH}/M_{bulge} ratio found in Marconi et al. (2004).

In Fig. 3, we plot the evolutionary tracks of the simulations in the SFR–BHAR parameter space along with the observational relationships. All the different models show similar variations in SFRs, over approximately two orders of magnitude (from 10s $M_\odot \, yr^{-1}$ to 0.1 $M_\odot \, yr^{-1}$), while the BHAR rates typically vary by around three orders of magnitude (from 0.1 $M_\odot \, yr^{-1}$ to $10^{-4} \, M_\odot \, yr^{-1}$). It is notable that the PNK models have a much larger variation in BHAR due to the exponential decay possible from the accretion disc reservoir.
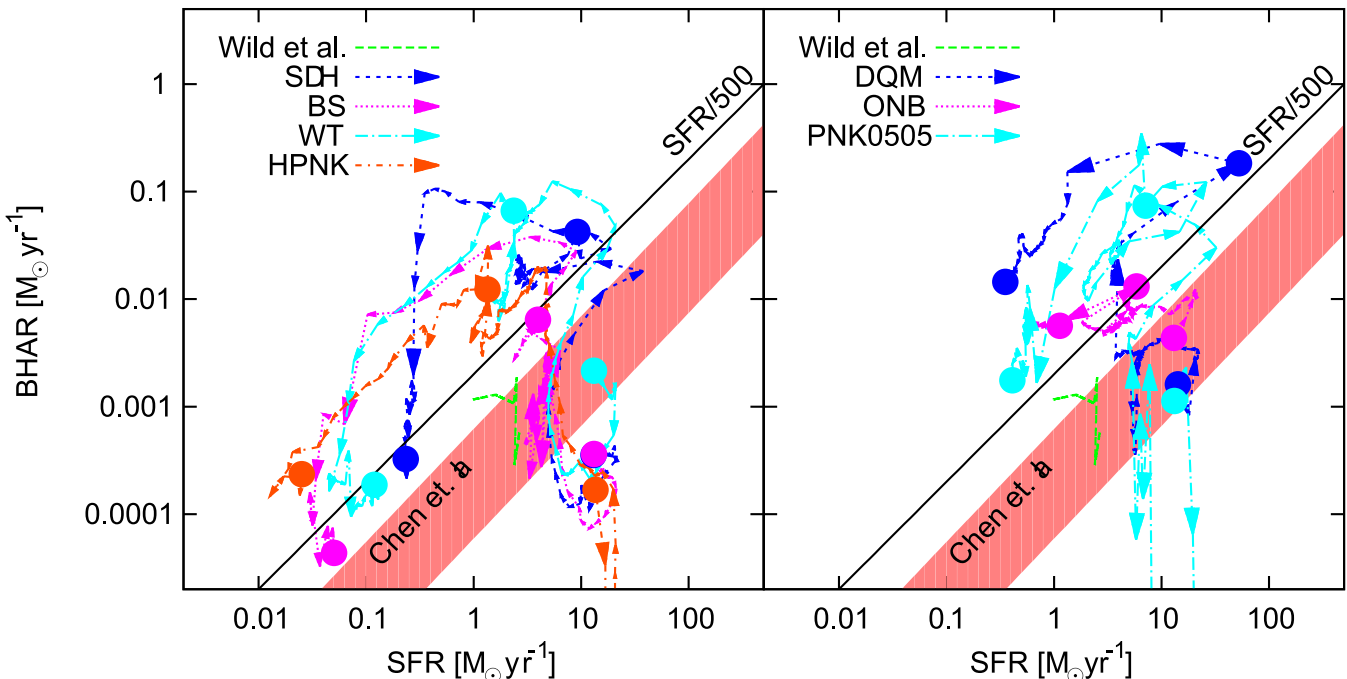

Figure 3. Evolution of the different models in the BHAR–SFR parameter space. The left-hand panel displays models that rely on the Bondi–Hoyle accretion or a variant of it, while the right-hand panel displays models using alternative accretion approaches. Also shown is the evolution inferred from the Wild et. al. (2010) data, the Chen et al. (2013) correlation and the SFR/500 line derived from the M_{BH}/M_{bulge} ratio found in Marconi et al. (2004). The evolution steps are averaged over 20 Myr periods, with each arrow corresponding to evolution in that period. Longer arrows thus represent correspondingly larger movements in the parameter space for a given period of time. The beginning, core-merger at 980 Myr and final output at 1.5 Gyr are all marked with the appropriately coloured circle (note SDH and BS have overlapping starting positions). Most models evolve through a small loop down and then upwards towards the top right first as the initial conditions settle and later as the system reaches core-merger. This is followed by a trend to the lower left once the system has become starved of fuel for further star formation or black hole accretion. The notable exception to this behaviour is the ONB model which has a very narrow range in BHAR throughout the simulation.

In the log–log parameter space plot the evolution of the different models is qualitatively similar (with the ONB radio-mode behaving in an expectedly different manner). The simulations start with a comparatively high SFR ($10\,\mathrm{M_\odot}\,\mathrm{yr}^{-1}$) due to the onset of cooling at the beginning of the simulation, and are accompanied by modest BHAR values ($10^{-3}\,\mathrm{M_\odot}\,\mathrm{yr}^{-1}$), placing the models in the lower right to middle of the parameter space. For some of the models (notably SDH, BS, WT and HPNK) there is a small initial fall in the BHAR prior to first periapsis, but this is then followed by an increasing BHAR (slightly under $0.01\,\mathrm{M_\odot}\,\mathrm{yr}^{-1}$) as the instabilities promoted during the initial pass are excited. This produces evolution that loops upwards towards the upper right of the diagram.

During the core merger both the BHAR and SFR rise although the increase in SFR can be quite weak depending upon the strength of the AGN feedback and the amount of gas available for star formation. At core-merger BHAR values range between $0.01\,\mathrm{M_\odot}\,\mathrm{yr}^{-1}$ and $0.1\,\mathrm{M_\odot}\,\mathrm{yr}^{-1}$, while the SFR values range between $1\,\mathrm{M_\odot}\,\mathrm{yr}^{-1}$ and 10s $\mathrm{M_\odot}\,\mathrm{yr}^{-1}$. Post merger, the systems decline in both the SFR and BHAR value and there is a trend diagonally down and left, which follows a close to linear correlation for a number of models (e.g. BS, WT, DQM and especially HPNK), albeit at a higher normalization than either the Chen et al. (2013) band or SFR/500 line.

In the ONB model the AGN feedback energy is channelled directly into the halo, and does not impact the nuclear gas or SFR significantly (the SFR varies by approximately 1.5 orders of magnitude). This lack of nuclear feedback, combined with the assumed accretion model, means that the BHAR is comparatively constant over time. While this behaviour is very different from other models, it is interesting to note that ONB spends more time closer to the average track predicted by the Wild et al. (2010) data than any of the other simulations although it is difficult to draw quantitative conclusions from this similarity.

4.2.2 Time-averaged correlations for the entire galaxies

We next quantify the evolution by evaluating correlations between the SFR and BHAR and compare directly to the ensembled-derived Chen et al. (2013) relationship with $\beta = 1.05 \pm 0.33$. Time averages weight all points along the evolutionary track equally and are less impacted by sudden rapid movements in the parameter space. Given the complexity of the evolutionary tracks over the entire merger simulation, it is clear that linear relationships, as in Chen et al. (2013), are unlikely to be recovered. However, breaking the evolution into pre- and post-merger provides a helpful subdivision as it isolates similar evolutionary epochs. In the analysis below we consider average values and ranges across the models, although we do not suggest that the average value across models has any specific meaning, rather it identifies trends in the correlations across the different models at different epochs.

We use outputs exactly spaced 5 Myr apart to calculate correlations, except HPNK which, due to disc space limits, were 10 Myr apart. As in Chen et al. (2013) we construct four bins in the SFR; however, we use a constant sample size in each bin, and the bin means are calculated via an arithmetic mean (see their equation 4). Variances in the means are then bootstrapped and used in the χ^2-minimization linear (log space) regression fitting. The fits that we find, along with their standard errors and χ^2 values, are summarized in Table 2 and plotted in Figs 4 and 5.

Examining the fits across the entire simulation given in Table 2 we find that some χ^2 values are poor (particularly DQM, ONB and PNK0505). Visual examination shows that residuals can be tub

Table 2. The time-averaged total SFR–BHAR correlations for different AGN feedback models, for different epochs of the simulations. The best-fitting parameters α and β correspond to $\log(\mathrm{BHAR}) = \alpha + \beta \times \log(\mathrm{SFR})$.

Model	α	β	χ^2	Epoch
SDH	-1.89 ± 0.21	-0.26 ± 0.44	0.05	All
BS	-2.75 ± 0.15	0.20 ± 0.28	0.83	All
WT	-2.11 ± 0.09	0.47 ± 0.15	9.67	All
HPNK	-2.41 ± 0.09	0.09 ± 0.20	4.90	All
DQM	-1.66 ± 0.06	-0.25 ± 0.16	12.62	All
ONB	-2.35 ± 0.02	-0.14 ± 0.05	27.06	All
PNK0505	-2.13 ± 0.06	0.76 ± 0.16	1.57	All
SDH	-2.23 ± 0.16	-0.32 ± 0.41	10.99	Pre-merger
BS	-2.93 ± 0.29	-0.13 ± 0.41	0.22	Pre-merger
WT	-2.16 ± 0.07	0.28 ± 0.22	6.75	Pre-merger
HPNK	-2.42 ± 0.10	-0.63 ± 0.28	13.03	Pre-merger
DQM	-2.44 ± 0.31	0.01 ± 0.50	0.93	Pre-merger
ONB	-2.54 ± 0.04	0.25 ± 0.10	0.99	Pre-merger
PNK0505	-1.98 ± 0.06	-0.01 ± 0.22	6.80	Pre-merger
SDH	-2.03 ± 0.28	1.07 ± 0.45	10.92	Post-merger
BS	-2.46 ± 0.20	1.10 ± 0.17	5.51	Post-merger
WT	-1.35 ± 0.26	1.54 ± 0.30	0.51	Post-merger
HPNK	-1.94 ± 0.23	0.87 ± 0.25	0.77	Post-merger
DQM	-1.38 ± 0.07	0.61 ± 0.24	3.49	Post-merger
ONB	-2.25 ± 0.00	-0.01 ± 0.02	1.23	Post-merger
PNK0505	-2.08 ± 0.08	1.25 ± 0.19	3.65	Post-merger

shaped in many cases, which is to be expected given the shape of the evolutionary tracks. In terms of the fitted slopes, the mean and range across all simulations is given by $\beta = 0.12^{+0.64}_{-0.38}$ although most models fall around zero, with SDH, DQM and ONB being slightly negative, while BS, WT, HPNK and PNK0505 are positive.

For the pre-merger evolution, there is a smaller spread in fitted slopes, with the mean and range (ONB neglected as having little variation) being $\beta = -0.08^{+0.36}_{-0.55}$. This indicates that rapid evolution up to higher BHAR values just prior to the core merger does not influence the time average significantly. The WT model is the notable positive slope outlier ($\beta = 0.28 \pm 0.22$) while the HPNK model has the largest negative slope at $\beta = -0.63 \pm 0.50$ although the standard error is large. The HPNK fit is clearly influenced by the right-most point that comes from the very low accretion values that are possible in this model.

For the post-merger evolution, with the exception of ONB, all the models have positive slopes, with a mean and range of $\beta = 0.91^{+0.63}_{-0.92}$. If we neglect the ONB model as a significant outlier, then the mean and range is notably tighter at $\beta = 1.07^{+0.47}_{-0.46}$. Most of the models using Bondi–Hoyle accretion approaches (SDH, BS, WT, HPNK) all produce slopes close to, or above, unity, as does PNK0505. DQM has a somewhat less steep slope at $\beta = 0.61 \pm 0.24$, but this value is still considerably steeper than either the pre-merger or full evolution values for this model. Thus with the exception of ONB, and within the bounds of error, all the post-merger correlations match the Chen et al. (2013) power law.

4.3 Correlations of spatially decomposed SFRs and BHARs

Given that the SFR and BHAR both have a strong dependence on the availability of cold gas, it is reasonable to expect stronger correlations between the nuclear SFR and BHAR than star formation in the extended regions of the galaxy. To define regions, we separate the nuclear and extended star formation by 1 kpc radial aperture cut-off. This is in agreement with the middle bin
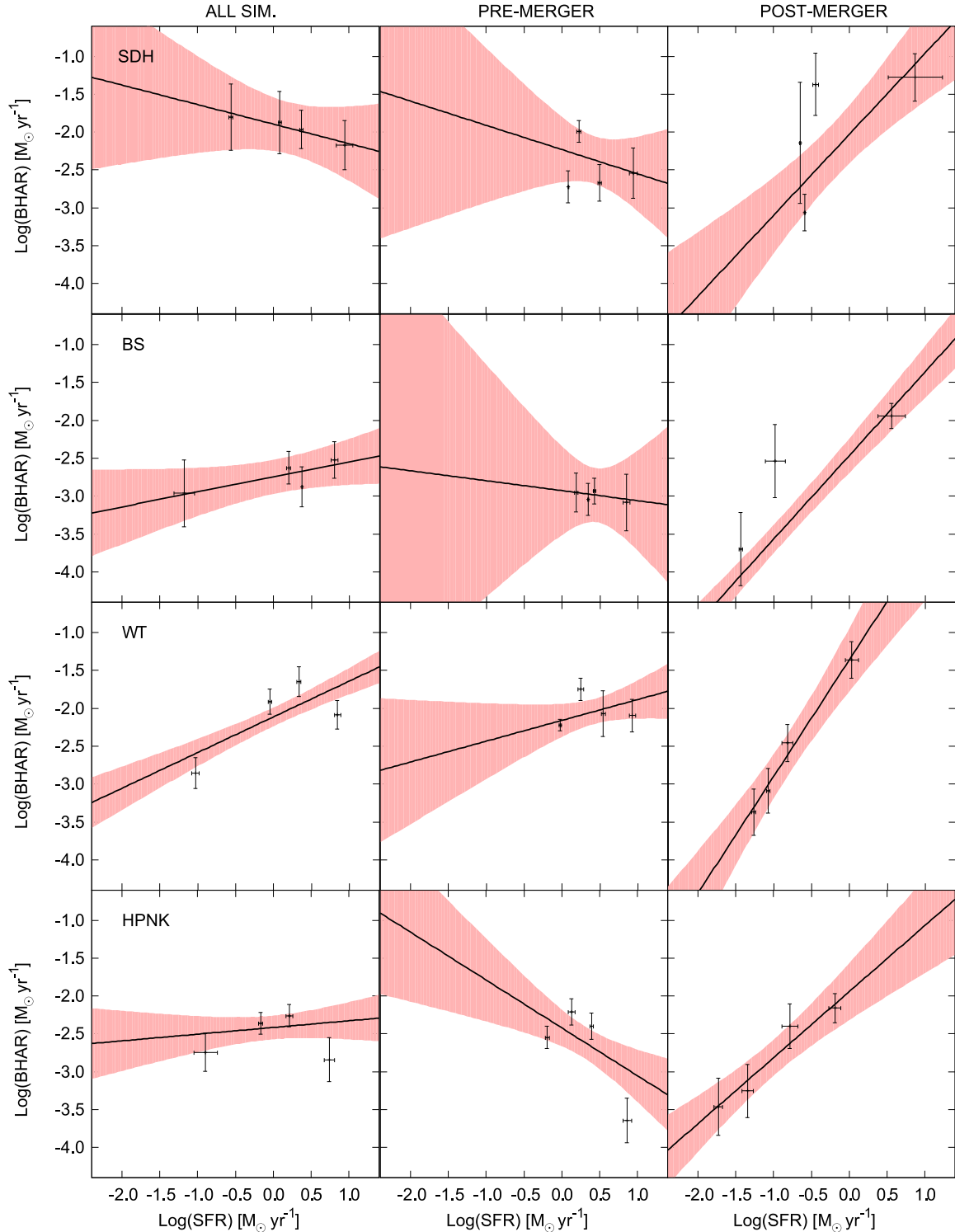
Figure 4. Time-averaged correlations between the total SFR and BHAR for the models that use the Bondi–Hoyle accretion or some variant of it. Results are given for three different epochs, all the simulation, the pre-merger evolution and the post-merger evolution. Error bars correspond to variances in the means and the dotted lines denote 95 per cent confidence bands around each fit. Four points are given in each plot and correspond to match the binning approach chosen in Chen et. al. (2013), with the values used in each bin coming from simulation outputs spaced 5 Myr apart (10 Myr in the case of HPNK).

considered by DSR12 but slightly smaller in scale than the minimum 1.7 kpc value used by LaMassa et al. (2013), which varied up to 3.5 kpc with galaxy redshift, due to the fixed size of the SDSS spectroscopic fibre. We note that the correlations in the literature have been reported in a reversed form to Chen et al. (2013), i.e. as

$SFR_{nuclear} \propto (BHAR)^{\beta_1}$. For this format, DSR12 report an exponent of $\beta_1 = 0.61^{+0.15}_{-0.11}$ for the 1 kpc cut-off, while LaMassa et al. (2013) report an exponent of $\beta_1 = 0.36 \pm 0.04$. Note that a decomposition of the DSR12 data into different aperture radii has a trend of decreasing exponent with increasing aperture radius, albeit at the cost of the
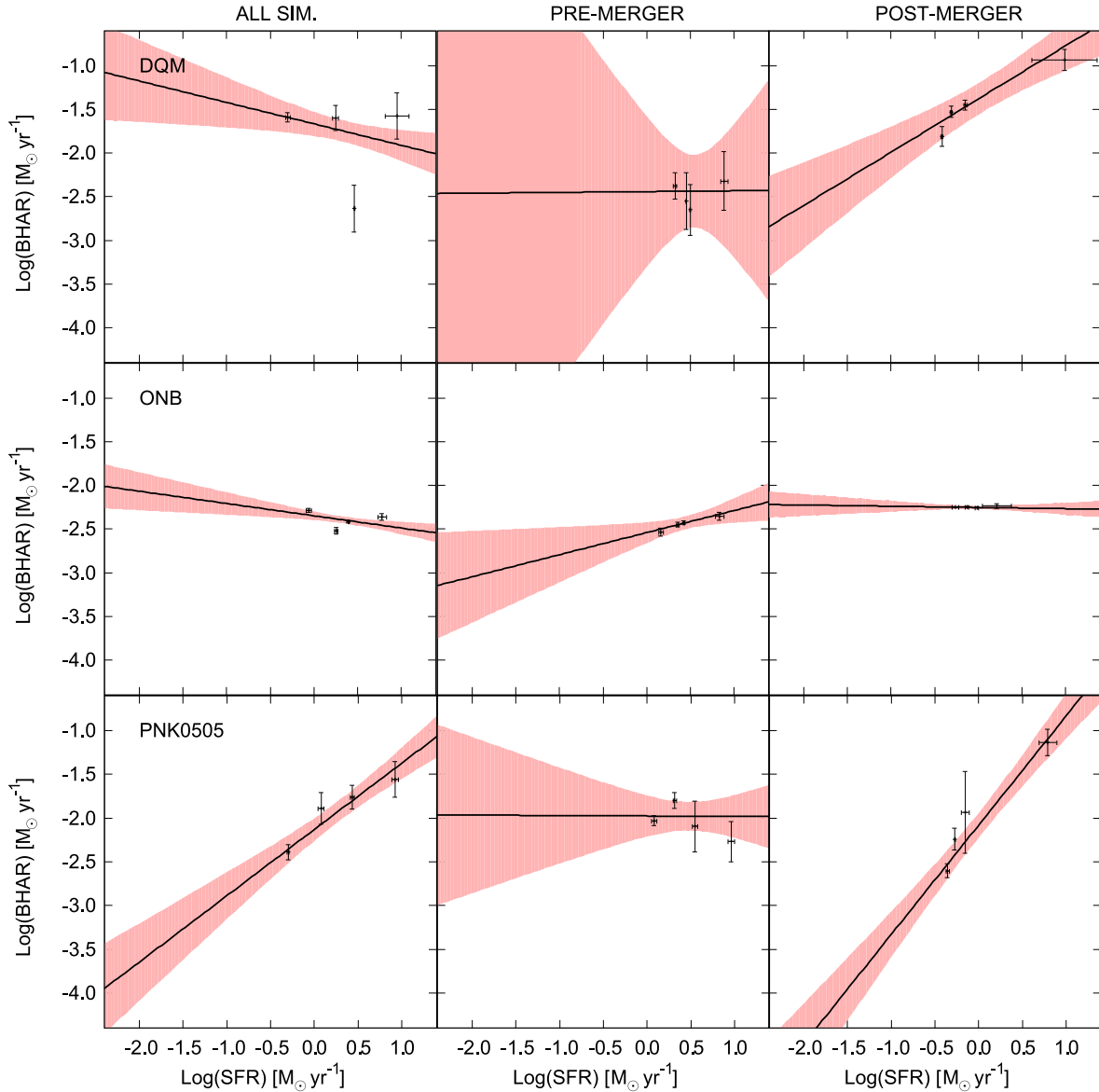
Figure 5. Time-averaged correlations between the total SFR and BHAR for the models that do not use the Bondi–Hoyle approach for calculating accretion. All other details are as in Fig. 4.

smaller radii not including 24 μm continuum, which could lead to a systematic bias. For the extended star formation they find $\beta_1 = 0.57^{+0.28}_{-0.17}$, which is still somewhat higher than the nuclear correlation found by LaMassa et al. (2013). Taken together these two results do indicate a stronger correlation of nuclear star formation with the BHAR, than for extended star formation, as would be expected.

To calculate the results for the spatially decomposed regions we have followed the correlation approach of DSR12, but in the absence of errors on the SFR and BHAR measurements we apply a (log-space) least-squares approach to calculate the best-fit, rather than using the Bayesian methodology of DSR12. However, using this approach introduces some problems for the simulations in that exponentially low or zero values tend to influence trends strongly. While approaches such as 'Cook's D' can be used to determined which outliers weight most strongly, we have taken a conservative approach of removing zero values and any BHAR and SFR values lower than 10^{-6} $M_\odot yr^{-1}$. While admittedly somewhat arbitrary,

we believe this approach provides the best way of determining the correlations of low to moderate activity. The amount of data removed is given in Table 3, and we denote whether data were removed due to low SFRs or BHARs by an s or b subscript. Only three models were impacted, WT, HPNK and PNK0505, mostly with less than 10 per cent of the data being impacted.

To provide rough visual guidelines on the accuracy of the fits we have also calculated confidence bands. Lastly, we note that the high activity episodes of the pre-merger galaxies are better analogues to the observed Seyfert sample (DSR12) than the post-merger remnant, but we include all data for completeness.

4.3.1 Nuclear regions

For this analysis, we present least-squares fits in Table 3. The raw simulation data are plotted in Figs 6 and 7, along with the fits and confidence bands.

Table 3. The time-averaged BHAR nuclear–SFR correlations for different AGN feedback models, for different epochs of the simulations. Parameters are reversed compared to Table 2, in that the best-fitting parameters α_1 and β_1 correspond to $\log(\text{SFR}) = \alpha_1 + \beta_1 \times \log(\text{BHAR})$.

Model	α_1	β_1	Per cent outliers	Epoch
SDH	0.34 ± 0.09	0.19 ± 0.03	0	All
BS	0.79 ± 0.15	0.32 ± 0.04	0	All
WT	1.51 ± 0.22	0.86 ± 0.08	6_s	All
HPNK	1.03 ± 0.21	0.59 ± 0.07	9_b	All
DQM	-0.12 ± 0.08	0.04 ± 0.03	0	All
ONB	-0.98 ± 0.28	-0.37 ± 0.11	0	All
PNK0505	0.50 ± 0.08	0.29 ± 0.03	10_b	All
SDH	0.56 ± 0.10	0.22 ± 0.03	0	Pre-merger
BS	0.23 ± 0.09	0.08 ± 0.02	0	Pre-merger
WT	0.47 ± 0.09	0.24 ± 0.03	0	Pre-merger
HPNK	0.32 ± 0.10	0.24 ± 0.04	9_b	Pre-merger
DQM	0.07 ± 0.13	0.08 ± 0.05	0	Pre-merger
ONB	-0.91 ± 0.36	-0.34 ± 0.14	0	Pre-merger
PNK0505	0.19 ± 0.10	0.13 ± 0.04	18_b	Pre-merger
SDH	0.12 ± 0.17	0.19 ± 0.06	0	Post-merger
BS	0.84 ± 0.21	0.51 ± 0.05	0	Post-merger
WT	2.22 ± 0.18	1.60 ± 0.06	17_s	Post-merger
HPNK	1.21 ± 0.37	0.83 ± 0.12	8_b	Post-merger
DQM	1.39 ± 0.12	1.14 ± 0.08	0	Post-merger
ONB	10.50 ± 2.83	4.75 ± 1.26	0	Post-merger
PNK0505	1.26 ± 0.10	0.68 ± 0.04	0	Post-merger

With the exception of the ONB model, we find positive correlations between the SFR and BHAR for all models across all epochs. For the entire simulation period, we find an average for the positive slopes (i.e. excluding the ONB model) of $\beta_1 = 0.38^{+0.48}_{-0.34}$. This is somewhat lower than the value reported by DSR12 of $\beta_1 = 0.61^{+0.15}_{-0.11}$ but similar to the LaMassa et al. (2013) value of $\beta_1 = 0.36 \pm 0.04$. Of course individual models do, however, vary considerably away from this mean value with the WT model having the steepest slope of $\beta_1 = 0.86 \pm 0.08$ and the DQM model having the shallowest slope at $\beta_1 = 0.04 \pm 0.03$.

For the post-merger systems, in agreement with the entire galaxy analysis, we find correlations that are closer to linear with an average and range across models of $\beta_1 = 0.83^{+0.78}_{-0.64}$. Notably, SDH is unusual in that its post-merger slope, $\beta_1 = 0.19 \pm 0.06$, is the same as the value for the entire simulation. This value is also the lowest slope for the post-merger systems. The high outlier is again WT with $\beta_1 = 1.60 \pm 0.06$. With exception of SDH and BS, the post-merger slopes are greater than DSR12.

For the positive slope pre-merger systems we find a shallow slope with comparatively little variation, with the mean and range across models being $\beta_1 = 0.17^{+0.07}_{-0.09}$. BS and DQM have the shallowest slopes with a $\beta_1 = 0.08$ value, while WT and HPNK share the steepest slope at $\beta_1 = 0.24$. For the pre-merger systems over half the evolution occurs with SFRs around or below $1\,\mathrm{M}_\odot\mathrm{yr}^{-1}$, while the BHAR evolves comparatively rapidly. The slight differences in the slope value can be traced to differences in SFR activity. For example, DQM stabilizes the galaxies against bar formation and thus keeps SFRs low, similarly BS has a small amount of early AGN activity that prevents higher SFRs. These models show the shallowest slopes. However, models with episodes of somewhat higher SFRs, e.g. WT, SDH, HPNK where the bar mode has moderate strength, show slightly steeper slopes.

The post-merger slope observed for the WT model is also interesting in the context of the appearance of voids around the black

hole (see Barai et al. 2014), as it has the largest void of all the models. These voids, typically of size up to 1 kpc in radius, but which are ultimately dependent on resolution (see fig. 13 in WT13b), can form as a product of the black hole influence/smoothing radius growing in size to encompass a sufficient number of neighbour particles. These voids can be produced in all models that follow the approach of increasing the black hole smoothing length to encompass a fixed number of neighbours (models SDH and BS, for example, both produce voids about 60 per cent the size of the WT model). In the merger simulations we describe the void is formed in the WT model about 200 Myr from the final time. Thus the slope clearly has the potential to be impacted.

However, the formation of the void in the WT model is not merely the result of the black hole growing larger and larger. Following the merger, a large amount of gas is heated into a fountain-like process and falls back down on to the nuclear regions around the 1.2 to 1.3 Gyr point. Visual inspection suggests that the void is larger in this model partly because the infalling material has a notable amount of angular momentum and naturally settles at radii beyond 1 kpc.

To assess the impact of voids we have examined the SFR and BHAR data in the WT run. The very lowest SFRs in the WT model are below the $10^{-6}\,\mathrm{M}_\odot\mathrm{yr}^{-1}$ cut-off we employ and correspond to the epoch when the void has formed (approximately half the SFR values during this period are zero, interspersed with non-zero values between $10^{-5}\,\mathrm{M}_\odot\mathrm{yr}^{-1}$ and $10^{-3}\,\mathrm{M}_\odot\mathrm{yr}^{-1}$). Including the zero values in the least-squares fit is not possible, but if we arbitrarily set the values to $10^{-10}\,\mathrm{M}_\odot\mathrm{yr}^{-1}$ this tilts the found power-law slope to $\beta_1 = 2.38 \pm 0.21$, from $\beta_1 = 1.60 \pm 0.06$. This demonstrates, at least for the WT model, that the void appears to have impacted the calculated correlation.

It is, however, important to determine if models without a significant void at all times can produce slopes that are equally steep, and whether there are any models with voids that, alternatively, produce shallow slopes. First, the DQM model which has an extremely small void (essentially smaller than the simulation resolution), with $\beta_1 = 1.14 \pm 0.08$, the second steepest slope after the WT model. While the BS model, which has a void slightly smaller than WT, has $\beta_1 = 0.51 \pm 0.05$, a comparatively shallow slope.

We thus conclude that the impact of the voids on the computed correlations is not necessarily larger than other physical properties such as the feedback model, and the overall effect seems model dependent. Undoubtedly some element of control should be placed upon these voids to stop them becoming too large. Methods have been suggested elsewhere (Barai et al. 2014).

4.3.2 Outer regions

Following the same analysis procedure as for the nuclear regions, we summarize the least-squares fits in Table 4. The raw simulation data are then plotted in Figs 8 and 9, along with the fits and confidence bands.

It is immediately striking that the pre-merger slopes are almost all negative (ONB is again an exception, but is poorly fit due to the narrow range in BHAR), with a mean and range of $\beta_1 = -0.29^{+0.14}_{-0.11}$. The most negative slope is the DQM model with $\beta_1 = -0.40 \pm 0.05$, while the least negative (excluding ONB) is BS with $\beta_1 = -0.15 \pm 0.03$. At this early stage of evolution the extended SFR is comparatively unimpacted by events in the nuclear region, and the Bondi–Hoyle variants have similar point distributions in the SFR–BHAR parameter space.
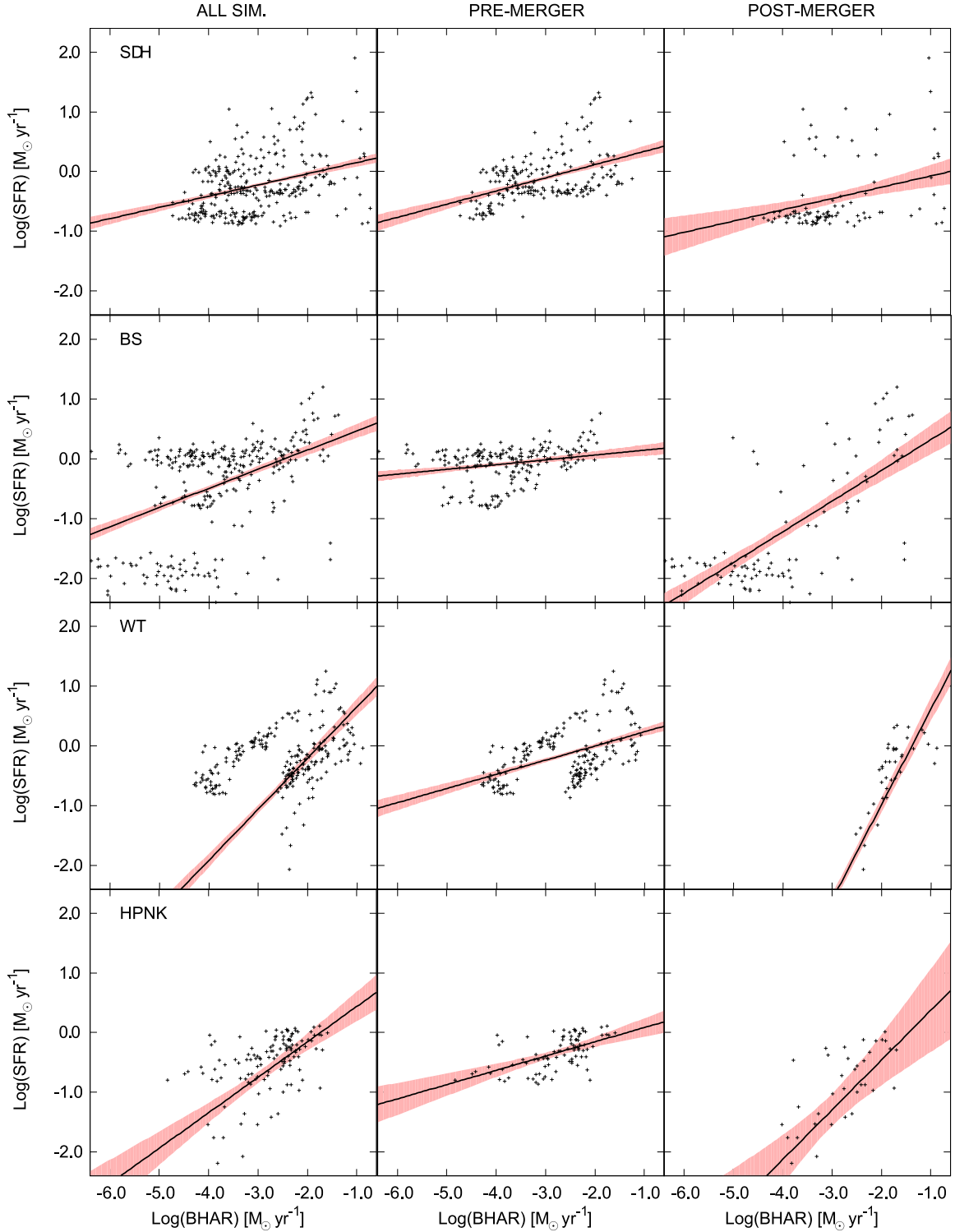
Figure 6. Time-averaged correlations between the BHAR and nuclear ($r < 1$ kpc) SFR for the models that use the Bondi–Hoyle accretion or some variant of it (note the different orientation of axes compared to Fig. 4). Each point corresponds to the instantaneous SFR and BHAR values from outputs spaced 5 Myr apart within the simulations (10 Myr in the case of HPNK). Results are given for three different epochs, all the simulation, the pre-merger evolution and the post-merger evolution. The filled red areas denote 95 per cent confidence bands around each fit.

Across the entire simulation the mean and range of the slopes are given by $\beta_1 = -0.18^{+0.22}_{-0.44}$. DQM has the most negative slope with $\beta_1 = -0.62 \pm 0.03$ while the least negative slope is BS which is slightly positive at $\beta_1 = 0.04 \pm 0.04$. Comparatively few of the models agree within errors.

For the post-merger analysis, most simulations only have a very narrow range in SFR and, again excluding ONB, we find a mean and range of $\beta_1 = 0.03^{+0.15}_{-0.16}$. The Bondi–Hoyle variants (SDH, BS, WT and HPNK) have slightly positive slopes while DQM and PNK0505 have exactly matching negative slopes, $\beta_1 = -0.13 \pm 0.02$.
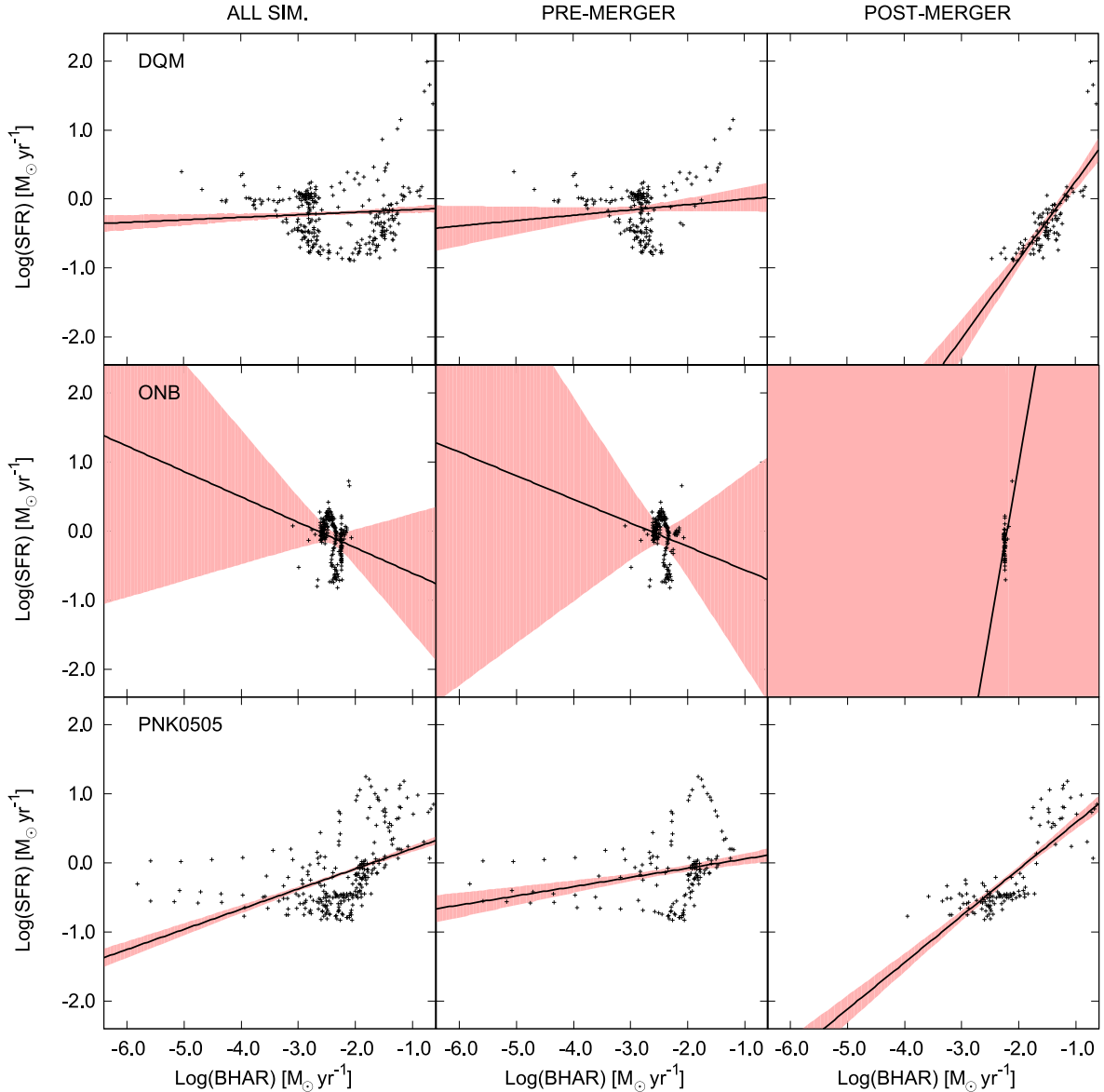
Figure 7. Time-averaged correlations between the BHAR and nuclear ($r < 1$ kpc) SFR for the models that do not use the Bondi–Hoyle accretion or some variant of it. All other details are as for Fig. 6. Note that for the ONB model the narrow range in BHAR means that the confidence bands are particularly large, the data would clearly be better fit if the axes were reversed.

However, overall the variation in the post-merger slopes is comparatively small. ONB again remains an outlier because there is so little variation in the BHAR value.

The negative slope for the pre-merger systems (ONB excluded) primarily arises from events during the period of first periapsis. At this time the disc is still fairly gas rich while the black hole has not grown significantly. This produces a relatively high SFR accompanied by a very low BHAR, in turn placing points in the upper left of the parameter space that end up producing a negative correlation. DQM shows slightly different behaviour at that time, but still produces a negative slope due to a number of comparatively high BHAR events that are accompanied by low SFR values.

The origin of the drop in the initial BHAR for models SDH, BS, WT, and HPNK can be traced to the change in the sound speed around the black hole. For these models there is an interaction between a high nuclear SFR and a small amount of thermal feedback from the AGN that drives up the sound speed of the gas surrounding

the black hole. Because the ONB model injects feedback into the halo, while the DQM model uses a kinetic boost and has little initial feedback, neither of these models introduce a significant temperature change in the initial configuration. The DQM model does have a notable change in the density around the black hole, but because the influence radius changes in response, the ratio of the surface density to the angular velocity does not fall significantly, and the accretion rate remains comparatively constant at these early stages.

4.4 Merger fractions and post-starburst black hole mass growth

We next consider the contribution of mergers to the black hole mass and the growth of the black hole following the core merger at 980 Myr of evolution. It is worth emphasizing that the mass growth mode in the simulations is precisely determined by the assumed

Table 4. The time-averaged extended SFR–BHAR correlations for different AGN feedback models, for different epochs of the simulations. Parameters are as in Table 2.

Model	α	β	Per cent outliers	Epoch
SDH	-0.84 ± 0.13	-0.19 ± 0.04	0	All
BS	-0.28 ± 0.18	0.04 ± 0.04	0	All
WT	-0.52 ± 0.12	-0.09 ± 0.04	0	All
HPNK	-0.44 ± 0.28	0.02 ± 0.09	9_b	All
DQM	-1.52 ± 0.06	-0.62 ± 0.03	0	All
ONB	-1.67 ± 0.57	-0.66 ± 0.24	0	All
PNK0505	-0.75 ± 0.08	-0.22 ± 0.03	10_b	All
SDH	-0.70 ± 0.11	-0.27 ± 0.03	0	Pre-merger
BS	-0.46 ± 0.14	-0.15 ± 0.03	0	Pre-merger
WT	-0.85 ± 0.08	-0.37 ± 0.03	0	Pre-merger
HPNK	-1.07 ± 0.18	-0.38 ± 0.06	9_b	Pre-merger
DQM	-0.84 ± 0.14	-0.40 ± 0.05	0	Pre-merger
ONB	2.71 ± 0.59	1.06 ± 0.24	0	Pre-merger
PNK0505	-0.29 ± 0.04	-0.18 ± 0.02	18_b	Pre-merger
SDH	-0.83 ± 0.04	0.08 ± 0.01	0	Post-merger
BS	-0.88 ± 0.07	0.16 ± 0.02	0	Post-merger
WT	-0.96 ± 0.04	0.04 ± 0.01	0	Post-merger
HPNK	-0.95 ± 0.10	0.18 ± 0.03	8_b	Post-merger
DQM	-0.94 ± 0.04	-0.13 ± 0.02	0	Post-merger
ONB	-6.63 ± 1.96	-2.60 ± 0.87	0	Post-merger
PNK0505	-0.98 ± 0.05	-0.13 ± 0.02	0	Post-merger

accretion law, be it Bondi–Hoyle or drag, or viscous accretion. Since the star formation algorithm does not account for mass loss into the ISM, which could subsequently be accreted on to the black hole, this mode of mass growth is not included.

For the merger fractions there is a maximum upper limit to the value determined in the simulations. If two equal-mass black holes merged and then there was no post-merger mass growth, the merger contribution is 50 per cent. Examining Table 5 shows that models with little post-merger mass growth (e.g. WT, PNK0505) follow this trend and have comparatively high merger fractions. Models that exhibit extensive post-merger mass growth, particularly DQM and SDH, instead show comparatively small merger fractions. The range of values we find, namely from ~10 to ~40 per cent, is consistent with the growing expectation that for black hole masses below $10^9\,\mathrm{M}_\odot$ mergers do not play a dominant role in mass growth (e.g. Anglés-Alcázar et al. 2013; Dubois, Volonteri & Silk 2013; Kulier et al. 2013; Volonteri & Ciotti 2013). However, what is perhaps surprising is the factor of 4 variation between models despite almost all of them matching the M–σ relationship.

The post-merger mass growth rates do show considerable variation (approximately a factor of 3.5 between the lowest and highest values), and most are higher than the average post-starburst mass growth value of 5 per cent inferred by Wild et al. (2010). The merger simulation is not, however, markedly distinct from their chosen sample. The simulated black hole masses are at the upper limit of their inferred mass range of $10^{7.5}\,\mathrm{M}_\odot$ and the merger remnant stellar morphology is a very flattened ellipsoid that nonetheless does fall above their stellar mass surface density cut-off of $\mu^* > 3 \times 10^8\,\mathrm{M}_\odot\mathrm{kpc}^{-2}$. Black hole luminosities for the merger also peak within, but at the upper end of their range at $10^{44}\,\mathrm{erg\ s}^{-1}$.

5 CONCLUSION

We have presented a detailed analysis of the evolution of AGN feedback models in the BHAR–SFR parameter space and contrasted the time-averaged trends in this space to observed relationships for ensembles of galaxies. In addition to models considered in WT13a and WT13b we have also added an additional model, described in HPNK12. Our principal conclusions are as follows.

(i) For the parameters we considered, the revised accretion model of HPNK produces significant early growth in the black hole masses, but produces considerably less growth at late times. The resulting final black hole mass is 1.4 standard deviations below the mean of the Gültekin et al. (2009) M–σ relationship, but still higher than other notable models e.g. BS. Due to the lack of late time growth in the black hole mass, this model also has the largest mass contribution from mergers, albeit only slightly larger than the WT model.

(ii) Evolution of a single merger system in the SFR–BHAR parameter space is highly complex even when averaged over 20 Myr periods. While a number of the models, especially those using variants of the Bondi–Hoyle accretion, do follow qualitatively similar evolution, namely a vertical rise followed by a diagonal decay to lower SFR and BHAR values, the precise quantitative behaviours can be distinctly different. Notably, none of the models reproduces the inferred evolution from Wild et al. (2010), but without an ensemble of merger simulations of varying mass this result should not be over-interpreted.

(iii) When converted into time-averaged correlations, the SFR–BHAR evolution manifests in expected ways. The pre-merger and full simulation correlations are generally flat, but the post-merger evolution for all models bar ONB shows a distinct positive correlation, with some models being close to linear. However, the normalization of these periods of evolution lies above both the Chen et al. (2013) and SFR/500 relationships.

(iv) Breaking the star formation into nuclear and extended components reproduces the qualitative behaviour observed in observational work, namely that there is a stronger correlation between the nuclear SFR and BHAR, than there is between the outer SFR and the BHAR. There is also a distinctly stronger correlation for the post-merger nuclear SFR than the pre-merger, which would be interesting to probe observationally at the ensemble level. The different models do not, however, favour one particular observational result, although the mean of the models over the entire simulation, $\beta_1 = 0.38^{+0.48}_{-0.34}$, is surprisingly close to the LaMassa et al. (2013) value of $\beta_1 = 0.36 \pm 0.04$.

(v) The models show significant variation in the contribution of mergers to the final black hole mass. This variation is directly attributable to the amount of mass growth that occurs post-merger: those models with little mass growth (e.g. WT; PNK0505) obviously have large merger fractions. The post-merger mass growth values are usually considerably larger than that derived by Wild et al. (2010), although the simulated system is very much at the upper end of the mass range they consider. There may also be subtle timing issues here related to when the starburst occurs relative to the main merger.

While resolution issues are significant in AGN models, it is also equally important to understand the variance in evolution in the SFR–BHAR parameter space that occurs as a result of different merger trees. This could be examined effectively through multiple zoom simulations, although new high-resolution uniform volume simulations have reached the point where similar mass resolution to that considered here can be achieved. Adaptive-mesh refinement techniques also provide an interesting alternative route to high resolution, although mass resolution in the collisional part of the simulation must be carefully considered against the extremely high spatial resolution that can be achieved.
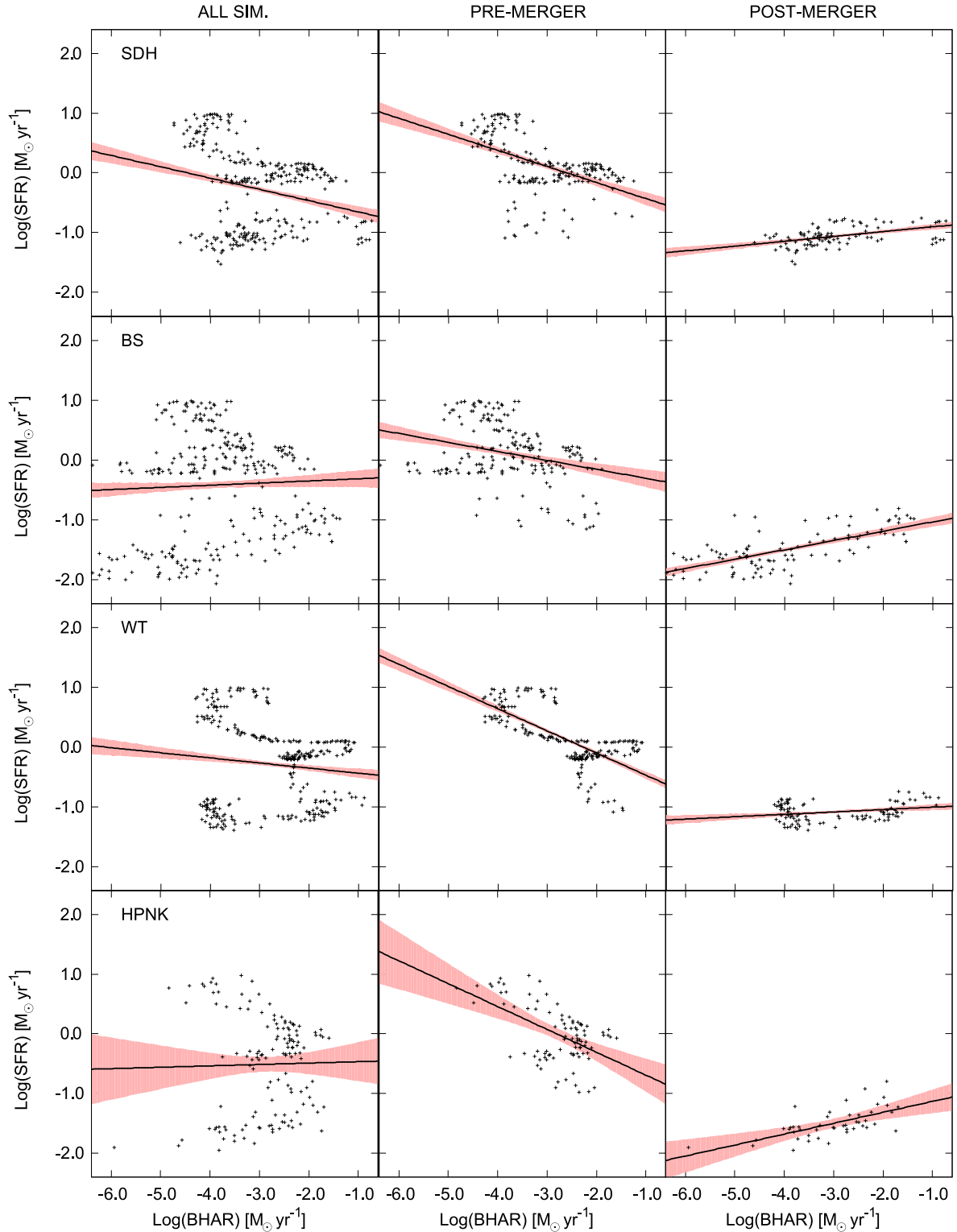
Figure 8. Time-averaged correlations between the BHAR and the 'outer' ($r > 1$ kpc) SFR for the models that use the Bondi–Hoyle accretion or some variant of it (note the different orientation of axes compared to Fig. 4). Results are given for three different epochs, all the simulation, the pre-merger evolution and the post-merger evolution. The filled red areas denote 95 per cent confidence bands around each fit.

Adding a full merger tree overcomes a number of issues (e.g. Moreno et al. 2013) related to the dynamics of isolated pairs of galaxies especially for lower mass systems. One possible area in which there may well be a distinct impact is related to the overall time AGN spend at a given luminosity (which we shall call the 'activity function'), which can be used in conjunction with halo population functions to estimate the luminosity function of AGN. Even though we have included hot haloes in our models, there is no representation of accretion of lower mass haloes that would typically be present in cosmological environments. Undertaking a
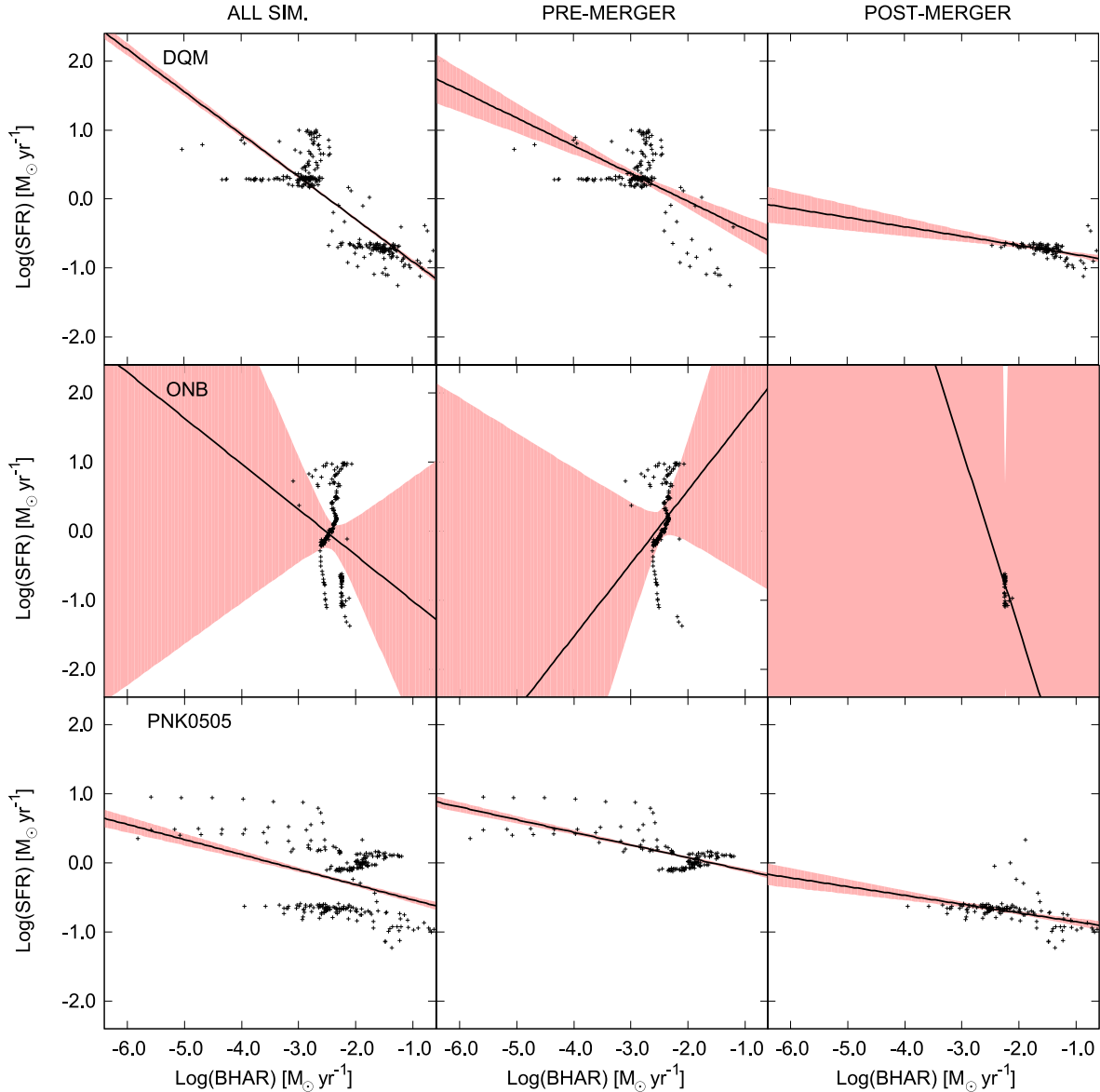
Figure 9. Time-averaged correlations between the BHAR and the 'outer' ($r > 1$ kpc) SFR for the models that do not use the Bondi–Hoyle accretion or some variant of it. All other details are as for Fig. 6. Note that for the ONB model the narrow range in BHAR means that the confidence bands are particularly large, the data would clearly be better fit if the axes were reversed.

Table 5. Final black hole masses, post-merger mass increase ratios and merger mass fractions for the different models. The ONB model is omitted as for reasons noted at the beginning of Section 4.

Model	Final mass/ $M_\odot$	Mass ratio	Merger fraction
BS	5.56×10^6	2.55	0.16[a]
SDH	2.52×10^7	3.80	0.13
WT	2.75×10^7	1.36	0.40
HPNK	8.80×10^6	1.20	0.42
DQM	3.32×10^7	4.94	0.08
PNK0505	3.81×10^7	1.66	0.36

[a]Note the merger fraction is estimated for the BS model as the black holes did not actually merge.

comparison of the activity function variance in different cosmological environments is clearly an important next investigation because determining whether any of the models spend an appreciable amount of time at lower luminosities, to match implied observational results,

is not yet well understood. In the theme of the current paper it is also worth investigating whether any of the models has a notable tail down to low luminosity in the isolated simulations. The model that stands out in this regard is PNK because of the presence of the exponential decay.

Lastly, while the current study has examined numerous different approaches to AGN feedback, it is important to remember that the evolution in the SFR–BHAR parameter space is also influenced by the precise SFR and stellar feedback algorithm. To this end, examining the impact of effective equation of state approaches on the evolution is also an important next step and one we plan to address with higher resolution simulations.

REFERENCES

Aird J. et al., 2010, MNRAS, 401, 2531

Alexander D. M., Hickox R. C., 2012, New Astron. Rev., 56, 93

Anglés-Alcázar D., Özel F., Davé R., Katz N., Kollmeier J. A., Oppenheimer B. D., 2013, preprint (arXiv:1309.5963)

Barai P., Viel M., Murante G., Gaspari M., Borgani S., 2014, MNRAS, 437, 1456

Bonfield D. G. et al., 2011, MNRAS, 416, 13

Booth C. M., Schaye J., 2009, MNRAS, 398, 53 (BS09)

Boyle B. J., Terlevich R. J., 1998, MNRAS, 293, L49

Chen C.-T. J. et al., 2013, ApJ, 773, 3

Costa T. et al., 2014, MNRAS

Debuhr J., Quataert E., Ma C.-P., 2011, MNRAS, 412, 1341 (DQM11)

Diamond-Stanic A. M., Rieke G. H., 2012, ApJ, 746, 168 (DSR12)

Dubois Y., Volonteri M., Silk J., 2014, MNRAS, 440, 1590

Ferrarese L., Merritt D., 2000, ApJ, 539, L9

Fioc M., Rocca-Volmerange B., 1997, A&A, 326, 950

Gabor J. M., Bournaud F., 2013, MNRAS, 434, 606

Gebhardt K. et al., 2000, ApJ, 539, L13

Gültekin K. et al., 2009, ApJ, 698, 198

Harrison C. M. et al., 2012, ApJ, 760, L15

Hayward C. C., Torrey P., Springel V., Hernquist L., Vogelsberger M., 2014, MNRAS, 442, 1992

Hickox R. C., Mullaney J. R., Alexander D. M., Chen C.-T., Civano F. M., Goulding A. D., Hainline K. N., 2014, ApJ, 782, 9

Hobbs A., Power C., Nayakshin S., King A. R., 2012, MNRAS, 421, 3443

Hopkins P. F., Hernquist L., 2009, ApJ, 698, 1550

Hopkins P. F., Quataert E., 2010, MNRAS, 407, 1529

Hopkins P. F., Hernquist L., Cox T. J., Di Matteo T., Robertson B., Springel V., 2006, ApJS, 163, 1

Katz N., 1992, ApJ, 391, 502

Kauffmann G. et al., 2007, ApJS, 173, 357

Kawakatu N., Umemura M., 2002, MNRAS, 329, 572

Kennicutt R. C., Jr, 1998, ApJ, 498, 541

King A., 2003, ApJ, 596, L27

Kormendy J., Ho L. C., 2013, AARA, 51, 511

Kulier A., Ostriker J. P., Natarajan P., Lackner C. N., Cen R., 2014, preprint (arXiv:1307.3684)

LaMassa S. M., Heckman T. M., Ptak A., Urry C. M., 2013, ApJ, 765, L33

Lutz D. et al., 2008, ApJ, 684, 853

Magorrian J. et al., 1998, AJ, 115, 2285

Marconi A., Risaliti G., Gilli R., Hunt L. K., Maiolino R., Salvati M., 2004, MNRAS, 351, 169

Moreno J., Bluck A. F. L., Ellison S. L., Patton D. R., Torrey P., Moster B. P., 2013, MNRAS, 436, 1765

Muldrew S. I., Pearce F. R., Power C., 2013, preprint (arXiv e-prints)

Newton R. D. A., Kay S. T., 2013, MNRAS, 434, 3606

Okamoto T., Nemmen R. S., Bower R. G., 2008, MNRAS, 385, 161 (ONB08)

Ostriker J. P., Choi E., Ciotti L., Novak G. S., Proga D., 2010, ApJ, 722, 642

Page M. J. et al., 2012, Nature, 485, 213

Power C., Nayakshin S., King A., 2011, MNRAS, 412, 269

Proga D., Kallman T. R., 2004, ApJ, 616, 688

Ragone-Figueroa C., Granato G. L., Murante G., Borgani S., Cui W., 2013, MNRAS, 436, 1750

Rosas-Guevara Y. M. et al., 2013, preprint (arXiv:1312.0598)

Sanders D. B., Soifer B. T., Elias J. H., Madore B. F., Matthews K., Neugebauer G., Scoville N. Z., 1988, ApJ, 325, 74

Serjeant S. et al., 2010, A&A, 518, L7

Shlosman I., Frank J., Begelman M. C., 1989, Nature, 338, 45

Sijacki D., Springel V., 2006, MNRAS, 366, 397

Silk J., Rees M. J., 1998, A&A, 331, L1

Silverman J. D. et al., 2008, ApJ, 679, 118

Springel V., Hernquist L., 2003, MNRAS, 339, 289

Springel V., Di Matteo T., Hernquist L., 2005, MNRAS, 361, 776 (SDH05)

Stinson G., Seth A., Katz N., Wadsley J., Governato F., Quinn T., 2006, MNRAS, 373, 1074

Tescari E., Katsianis A., Wyithe J. S. B., Dolag K., Tornatore L., Barai P., Viel M., Borgani S., 2014, MNRAS, 438, 3490

Thacker R. J., Couchman H. M. P., 2000, ApJ, 545, 728

Thacker R. J., Scannapieco E., Couchman H. M. P., 2006, ApJ, 653, 86

Thomas P. A., Couchman H. M. P., 1992, MNRAS, 257, 11

Vogelsberger M., Genel S., Sijacki D., Torrey P., Springel V., Hernquist L., 2013, MNRAS, 436, 3031

Volonteri M., Ciotti L., 2013, ApJ, 768, 29

Wada K., Norman C. A., 2001, ApJ, 547, 172

Wild V., Heckman T., Charlot S., 2010, MNRAS, 405, 933

Williamson D. J., Thacker R. J., 2012, MNRAS, 421, 2170

Wurster J., Thacker R. J., 2013a, MNRAS, 431, 539 (WT13a)

Wurster J., Thacker R. J., 2013b, MNRAS, 431, 2513 (WT13b)

This paper has been typeset from a TEX/LATEX file prepared by the author.